

DATATRANSFER: NEURAL NETWORK-BASED INTERPOLATION ACROSS UNSTRUCTURED MESHES

JIAXIONG HAO[†], YUNQING HUANG[§], NIANYU YI[†]

ABSTRACT. This paper presents a neural network-based interpolation framework for transferring numerical approximations on different unstructured meshes. Traditional projection or interpolation techniques often depend on mesh connectivity, explicit element mappings, or local reconstruction procedures, which can be computationally demanding and sensitive to mesh misalignment. Instead, we formulate the problem as a data-driven regression task that predicts function values at arbitrary target locations from scattered nodal data on the source mesh. By systematically exploring and comparing several neural network architectures, we identify a configuration that balances accuracy and efficiency and that performs reliably across a range of mesh resolutions and topologies. The resulting model enables fast and accurate evaluation without requiring access to mesh connectivity or element-wise information. Numerical experiments on adaptive meshes suggest that the framework is effective for field reconstruction and data transfer tasks. The code used in this paper is publicly available on GitHub.¹

1. INTRODUCTION

Numerical simulations in engineering and applied sciences commonly rely on mesh-based discretizations of partial differential equations over complex domains. When multiphysics coupling, mesh adaptivity, or evolving geometries are involved, computations often require transferring data between non-matching meshes to maintain accuracy, consistency and stability. Multiphysics problems in particular demand distinct meshes for different physical fields due to varying geometric or physical constraints. For example, fluid domains typically require meshes that resolve boundary layers and accommodate large deformations, whereas solid domains emphasize geometric fidelity and material interfaces, as in fluid–structure interaction. In coupled structural–thermal analyzes, structural mechanics favors geometric conformity, while thermal diffusion demands fine resolution in regions of steep gradients [11]. Similar challenges appear in multigrid methods [15], global/local coupling [3] and domain decomposition [10], where information must be transferred across meshes of differing resolution or topology. These difficulties are further amplified in time-dependent simulations where meshes are regenerated to track moving interfaces or evolving features. Although adaptivity enhances accuracy and efficiency, it simultaneously creates a recurring need to project or interpolate the solution between successive meshes. Accurate and stable mesh-to-mesh data transfer has therefore become a fundamental requirement in numerical simulations [4, 21], yet designing schemes that preserve numerical properties across meshes remains a challenging task.

Interpolation strategies for mesh transfer fall broadly into two categories: mesh-based interpolation and mesh-free function reconstruction. Mesh-based methods include element-wise finite element interpolation, nearest-neighbor schemes, and local weighted averaging. They rely on the geometric and topological relationship between source and target meshes, requiring point-location queries to identify the containing element for each target point. As mesh size and complexity increase, especially in large-scale unstructured discretizations, this process becomes prohibitively expensive. Even with acceleration structures such as kd-trees or octrees, geometric queries often remain a dominant performance bottleneck. Moreover, these methods are sensitive to mesh quality and may exhibit discontinuities or reduced accuracy in regions of large deformation [19, 14]. Galerkin projection represents a more sophisticated mesh-based approach, ensuring consistency of physical quantities by integrating over mesh-defined regions with target basis functions. However, it requires constructing a supermesh and incurs substantial overhead from geometric

¹GitHub: <https://github.com/FEMmaster/DataTransfer>.

2020 *Mathematics Subject Classification.* 92B20, 65D05, 65M60.

Key words and phrases. Interpolation, Unstructured meshes, Neural networks, Extreme learning machine, Radial basis function.

preprocessing and integration over intersected domains. Mesh-free function reconstruction methods, such as radial basis function (RBF) interpolation [25], moving least squares (MLS) [16], and global polynomial fitting, construct smooth approximation functions from source mesh nodes for evaluation at arbitrary points. These methods yield smooth and numerically stable approximations independent of the target mesh topology, making them highly effective in dynamic or adaptive applications such as structural deformation, interface tracking, and mesh reconstruction.

Machine learning methods have recently gained traction as data-driven tools in scientific computing and engineering. Feedforward neural networks, in particular, have proven effective at approximating high-dimensional mappings from scattered samples, with applications ranging from PDE surrogate modeling [7] to image interpolation [22] and physical field reconstruction [26]. Much of the earlier work focused on environmental data interpolation [24, 1, 23, 27]; for example, [28] compared several machine-learning models for soil texture classification and interpolation of particle size distributions. On the theoretical side, [18] established that single-layer neural networks with n hidden neurons can exactly interpolate n distinct samples, while [2] showed that extreme learning machines (ELM) can mitigate the Runge phenomenon and substantially improve interpolation accuracy. Notably, Li and Chen [17] developed an efficient interpolation scheme based on radial basis functions for transferring data between truly unstructured grids in both two and three dimensions. Bucelli et al. [6] proposed the RL-RBF-G method, an extension of rescaled localized RBF interpolation that uses the geodesic distance to capture geometric and topological features of the domain and to improve robustness for data transfer in multiphysics problems. Chen and Cao [8] developed neural-network interpolation operators tailored for scattered data, providing error estimates and demonstrating their effectiveness in approximating multivariate functions. Their work demonstrated that RBF-based approaches could overcome the limitations of traditional linear interpolation, particularly in heterogeneous or non-matching discretizations. Despite these advances, the use of neural networks for transferring finite element solutions across non-matching meshes—particularly in adaptive or multiphysics contexts—remains largely unexplored. Motivated by this gap, we investigate neural network-based global regression strategies for mapping nodal values from a source mesh to arbitrary target meshes. Once trained on a function sampled from one mesh, the model generalizes to interpolate the same function on meshes of varying topology and resolution, bypassing mesh connectivity and element-wise search while maintaining accuracy and efficiency. Overall, this framework provides a flexible and scalable alternative to traditional interpolation techniques.

The remainder of this paper is organized as follows. [Section 2](#) begins with a formal problem formulation on non-nested triangular meshes in [Section 2.1](#). The section then introduces a sequence of neural-based surrogate models used to reconstruct piecewise linear solutions from scattered pointwise data. Specifically, [Section 2.2](#) investigates a standard fully connected neural network trained via gradient descent. [Section 2.3](#) presents an Extreme Learning Machine framework with fixed random projections and closed-form output weights, offering a significant speed-up, though its accuracy is limited by the distribution of training points. [Section 2.4](#) examines a Radial Basis Function augmented ELM architecture that improves approximation quality in the presence of nonuniform sampling. Each modeling approach is accompanied by representative numerical experiments, including tests on quasi-uniform and adaptive meshes. In the applications discussed in [Section 3](#), the RBF-ELM model is applied for iterative mesh-to-mesh data transfer. Lastly, [Section 4](#) concludes the paper with a brief summary and a discussion of potential extensions.

2. NEURAL NETWORK-BASED INTERPOLATION

Data transfer between unmatched meshes arises frequently in scientific computing. A typical instance occurs in time-dependent simulations with adaptive discretizations, where the solution from one step must be carried over to the mesh at the next in order to advance the computation. The demand becomes particularly critical in multiphysics problems, as different fields are often discretized separately and must exchange data to maintain consistent coupling. Traditional finite element interpolation relies on mesh-based procedures that require explicit geometric information. Alternatively, reformulating the task as a regression problem over scattered spatial data yields a continuous surrogate model, which not only approximates the finite element solution but also enables pointwise evaluation without reference to mesh connectivity. The discussion begins with a mathematical formulation of the interpolation task.

2.1. Problem Formulation. Let $\Omega \subset \mathbb{R}^d$ denote a bounded physical domain. We consider two finite element meshes of Ω : the source mesh $\mathcal{T}_A = (\mathcal{N}_A, \mathcal{C}_A)$ with nodal coordinates \mathcal{N}_A and element set \mathcal{C}_A , and analogously the target mesh $\mathcal{T}_B = (\mathcal{N}_B, \mathcal{C}_B)$. On the source mesh \mathcal{T}_A , we define the finite element space

$$V_h := \{v \in C^0(\Omega) : v|_K \in P_k(K), \forall K \in \mathcal{T}_A\},$$

which is a subspace of $H^1(\Omega)$ consisting of globally continuous functions that restrict to polynomials of degree at most k on each element. The finite element solution $u_h \in V_h$ admits the nodal representation

$$u_h(\mathbf{x}) = \sum_{i=1}^N u_i \phi_i(\mathbf{x}), \quad \mathbf{x} \in \Omega,$$

where $u_i \in \mathbb{R}$ denotes the solution value at node x_i and the basis functions satisfy $\phi_j(x_i) = \delta_{ji}$, ensuring $u_h(x_i) = u_i$ for all $x_i \in \mathcal{N}_A$. Additionally, u_h is assumed to be available at interior quadrature points of each element in \mathcal{C}_A . Note that u_h is readily evaluated at nodal and interior quadrature points since the quadrature points are fixed within each element, but evaluating at arbitrary locations requires nontrivial element search.

To circumvent this geometric search, a globally continuous surrogate $\tilde{u} : \Omega \rightarrow \mathbb{R}$ is introduced to approximate the discrete finite element solution $u_h(x)$ across the domain:

$$\tilde{u}(\mathbf{x}) \approx u_h(\mathbf{x}), \quad \forall \mathbf{x} \in \Omega.$$

Note that this surrogate model permits evaluation at arbitrary spatial locations and free from any geometric correspondence or mesh connectivity between \mathcal{T}_A and \mathcal{T}_B . Specifically, a discrete training dataset is available from the finite element solution u_h ,

$$\mathcal{D}_A = \{(\mathbf{x}_i, u_h(\mathbf{x}_i)) : \mathbf{x}_i \in \mathcal{S}_A\},$$

where the sample set \mathcal{S}_A is typically taken as the nodal points \mathcal{N}_A or possibly includes additional interior points (e.g., quadrature points). Based on this, the objective is to construct a parametric regression model $\tilde{u}(x; \theta)$ with parameters θ , such that

$$\tilde{u}_\theta(\mathbf{x}) \approx u_h(\mathbf{x}), \quad \forall \mathbf{x} \in \Omega,$$

The parameters θ are determined by solving the optimization problem:

$$\min_{\theta} \sum_{\mathbf{x}_i \in \mathcal{S}_A} (\tilde{u}_\theta(\mathbf{x}_i) - u_h(\mathbf{x}_i))^2.$$

Approximating scattered data with high-dimensional and nonlinear structure calls for a model class capable of representing complex relations. Among the wide range of models, feedforward neural networks provide a natural and compelling choice. However, a critical issue arises from the non-uniform sampling in \mathcal{S}_A induced by adaptive meshes where local refinement produces densely clustered nodes in some regions and sparse coverage in others. As a result, the interpolation accuracy of neural network surrogates may vary across the domain, reflecting both mesh complexity and sampling distribution. Building on the mesh-agnostic regression framework described above, the subsequent sections introduce a sequence of neural network models for transferring finite element solutions across non-nested adaptive meshes. Their evaluation considers the influence of sampling distributions on performance and emphasizes strategies that balance accuracy and computational efficiency.

2.2. Data Transfer via Feedforward Neural Network. Motivated by the universal approximation theorem [9], we employ a standard multilayer perceptron (MLP) as a baseline model to assess the capability of feedforward architectures for data transfer between finite element meshes. A general L -layer feedforward neural network is defined as a parameterized mapping $u_\theta : \mathbb{R}^{d_0} \rightarrow \mathbb{R}^{d_L}$. Let $\mathbf{x}^{(0)} := \mathbf{x}$ denote the input. For each layer $k = 1, \dots, L - 1$, the transformation is given by

$$\mathbf{x}^{(k)} = \Phi^{(k)}(\mathbf{x}^{(k-1)}) = \sigma(\mathbf{W}^{(k)} \mathbf{x}^{(k-1)} + \mathbf{b}^{(k)}),$$

where σ is an activation function, $\mathbf{W}^{(k)} \in \mathbb{R}^{d_k \times d_{k-1}}$ and $\mathbf{b}^{(k)} \in \mathbb{R}^{d_k}$ are trainable weight and bias matrices. The final layer omits activation in order to produce unrestricted real-valued outputs suitable for regression. Therefore, the network can be expressed as

$$\tilde{u}_\theta(\mathbf{x}) = \mathbf{W}^{(L)} \left(\Phi^{(L-1)} \circ \dots \circ \Phi^{(2)} \circ \Phi^{(1)}(\mathbf{x}) \right) + \mathbf{b}^{(L)}.$$

Given training samples $\{(\mathbf{x}_i, u(\mathbf{x}_i))\}_{i=1}^m$ drawn from the source mesh (e.g., nodal or quadrature points), the parameters are determined by minimizing the empirical mean squared error

$$\theta^* = \arg \min_{\theta} \frac{1}{m} \sum_{i=1}^m (u_\theta(\mathbf{x}_i) - u(\mathbf{x}_i))^2.$$

The structure illustrated in Figure 1 reflects the composition described above, comprising $L - 1$ hidden layers followed by a linear output layer. For the case of a two-dimensional input (x, y) , the first-layer weight matrix and bias vector take the form $\mathbf{W}^{(1)} = [w_{ij}] \in \mathbb{R}^{n \times 2}$ and $\mathbf{b}^{(1)} = [b_1, \dots, b_n]^T$, producing the hidden-layer output $\Phi^{(1)} = [\phi_1^1(x, y), \dots, \phi_n^1(x, y)]^T$. The final output layer yields a weighted combination of the hidden-layer activations,

$$\tilde{u}_\theta(x, y) = \mathbf{W}^{(L)} \Phi^{(L-1)} + \mathbf{b}^{(L)}, \quad \mathbf{W}^{(L)} = [u_1, \dots, u_n].$$

When the bias term is omitted (i.e., $\mathbf{b}^{(L)} = 0$), this structure bears a close resemblance to the coefficient-basis representation of finite element solutions.

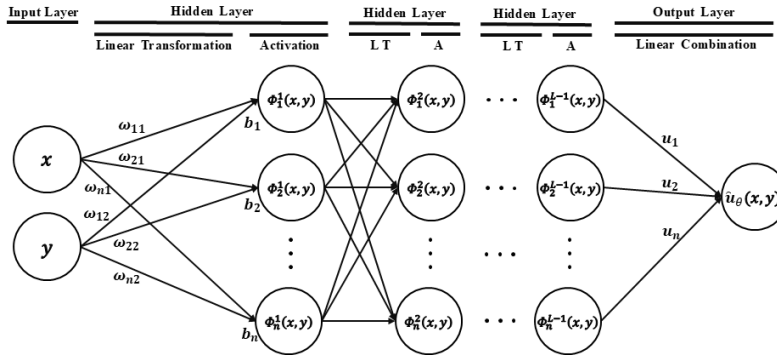


FIGURE 1. Schematic architecture of a fully connected feedforward neural network.

Throughout this section and those that follow, the interpolation accuracy is assessed using two standard metrics defined on the target mesh \mathcal{T}_B : the mean absolute error (MAE), which measures the average pointwise deviation between predicted and reference values, and the relative L^2 error (RL2), which quantifies the normalized energy difference between the prediction and the ground truth. Their discrete forms are given by

$$\text{MAE} = \frac{1}{M} \sum_{i=1}^M |\tilde{u}_\theta(\mathbf{x}_i) - u(\mathbf{x}_i)|, \quad \text{RL2} = \frac{\sqrt{\sum_{i=1}^M (\tilde{u}_\theta(\mathbf{x}_i) - u(\mathbf{x}_i))^2}}{\sqrt{\sum_{i=1}^M (u(\mathbf{x}_i))^2}},$$

where $\{\mathbf{x}_i\}_{i=1}^M$ denotes the evaluation points on the target mesh. The numerical experiments proceed by examining the performance of the neural network framework and begin with tests on a quasi-uniform mesh.

Example 2.1. *As a preliminary test of the transfer task, we consider a relatively high-frequency oscillatory function*

$$u(x, y) = \sin(5\pi x) \sin(5\pi y), \quad (x, y) \in [-1, 1]^2.$$

A network with three hidden layers of width 128 is used, yielding the architecture [2, 128, 128, 128, 1]. The activation function is $\sigma = \tanh$ and parameters are initialized by the Xavier uniform scheme. Training adopts a hybrid strategy: Adam is used for rapid initial descent, followed by L-BFGS refinement near local

minima, yielding more reliable convergence than either method alone; termination occurs once the loss stagnates or a prescribed iteration budget is reached.

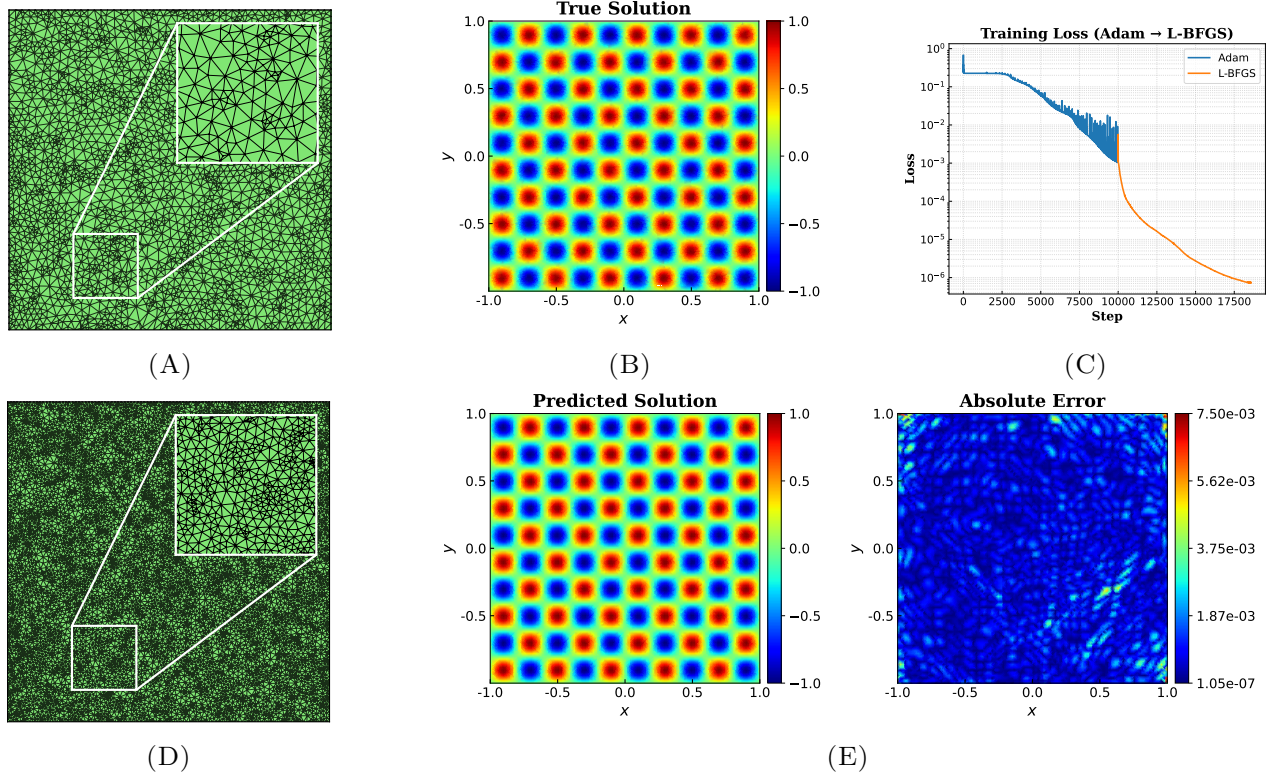


FIGURE 2. [Theorem 2.1](#), NN interpolation on a quasi-uniform mesh. (A) training mesh containing 2,500 nodes; (B) exact solution used as reference; (C) history of the training loss; (D) test mesh with 10,000 evaluation points; (E) interpolated solution together with the corresponding error distribution.

Figure 2 illustrates the overall training and testing results of the network on the oscillatory benchmark. The training dataset is drawn from the nodal points of a quasi-uniform mesh, shown in [Figure 2A](#), which contains approximately 2,500 nodes. [Figure 2B](#) presents the corresponding exact solution evaluated on this mesh. Owing to the limited mesh resolution, the solution appears sparse and lacks fine-scale features.

[Figure 2C](#) shows the training loss curve. The transition from oscillatory descent to a smoother decline marks the switch from Adam to L-BFGS optimization. The network converges to a local minimum after about 13,000 iterations. Beyond this point, the loss remains near 10^{-6} with additional training requiring much higher cost for only minor gains. The interpolation performance is further evaluated on finer meshes, as shown in [Figure 2D](#) and the corresponding interpolated solutions and error distributions are presented in [Figure 2E](#). Neural networks yield smooth approximations even when trained on relatively sparse data and the reconstructed solutions become visibly smoother when evaluated on finer grids than those used for training, whereas finite element interpolation lacks any improvement in smoothness by its piecewise linear nature, as will be shown in [Section 3](#). Mean absolute error stays near 10^{-3} under different hyperparameter choices and further enlarging the training set does not reduce this level but instead results primarily in smoother predicted fields with little gain in accuracy.

In contrast to the uniform mesh considered above, many practical simulations rely on adaptive mesh refinement to balance accuracy and efficiency. Such techniques increase resolution in regions of high complexity or large estimated error while coarsening in smoother areas, leading to a non-uniform distribution of nodes with dense clusters in some regions and sparse coverage elsewhere. Such adaptive strategies are particularly important for functions with sharp localized gradients or singularities. The next example

reflects this setting by considering a target function obtained from a finite element solution computed on an adaptively refined mesh.

Example 2.2. Let $\Omega = [-1, 1]^2$ and $T = (0, 1]$, consider the heat equation with Dirichlet boundary conditions

$$\begin{cases} \partial_t u - \Delta u = f, & \text{in } \Omega \times T, \\ u(\mathbf{x}, t) = g(\mathbf{x}, t), & \text{on } \partial\Omega \times T, \\ u(\mathbf{x}, 0) = u_0(\mathbf{x}), & \text{in } \Omega, \end{cases}$$

where the forcing term f is chosen such that

$$u(x, y, t) = \exp(-50((x - 0.5 \cos(2\pi t))^2 + (y - 0.5 \sin(2\pi t))^2))$$

is the exact solution, which serves as the reference in subsequent error evaluation. The boundary condition is prescribed as $g(x, y, t) = u(x, y, t)|_{(x, y) \in \partial\Omega}$, and the initial condition is given by $u_0(x, y) = u(x, y, 0)$. Training data \mathcal{T}_A are constructed from a representative snapshot of the adaptive numerical solution and its associated mesh. All hyperparameters are kept the same as in [Theorem 2.1](#) with the only change being a reduced network architecture of $[2, 64, 64, 64, 1]$.

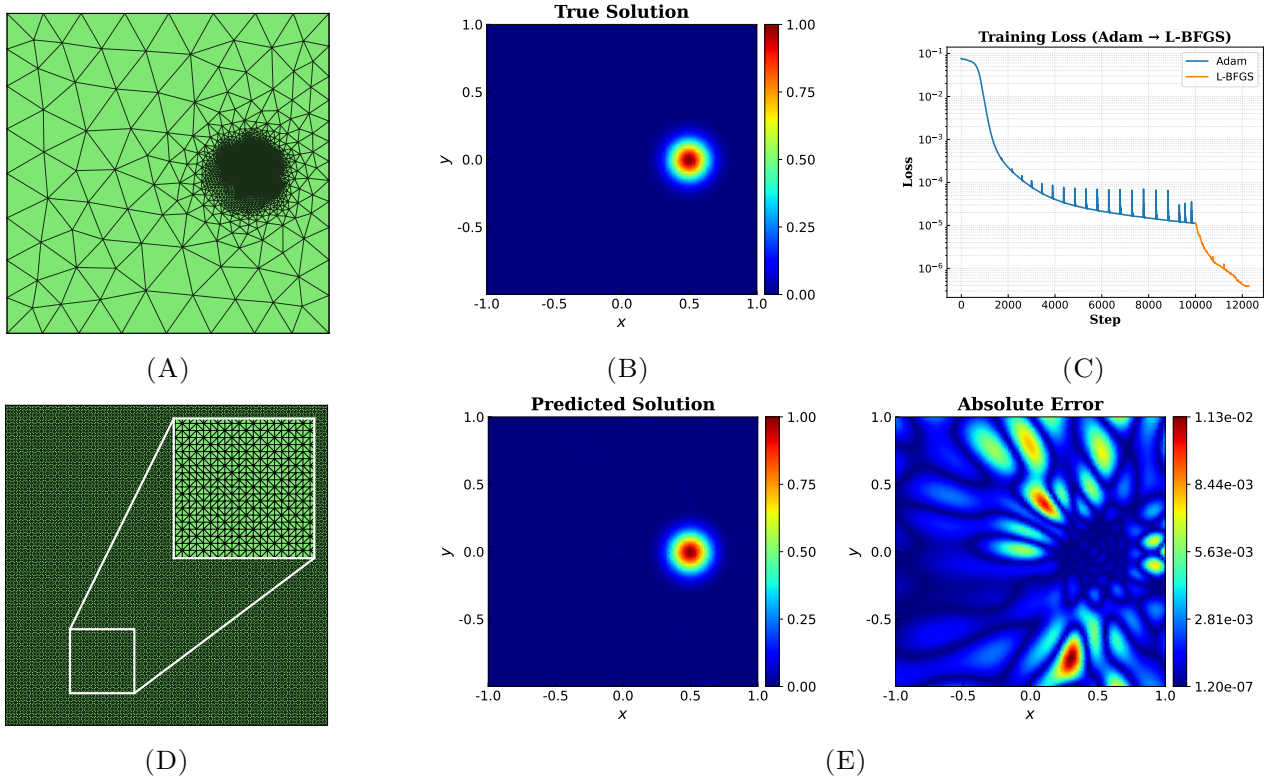


FIGURE 3. [Theorem 2.2](#), NN interpolation on an adaptive mesh. (A) training mesh; (B) reference solution; (C) history of the training loss; (D) test mesh with 10,000 evaluation points; (E) interpolated solution together with the corresponding error distribution.

Solved with adaptive finite element methods (see, e.g., [13]), the problem produces a series of numerical approximations accompanied by the corresponding adaptively refined meshes. Representative snapshots of the adaptive mesh and the corresponding finite element approximation are displayed in [Figure 3A](#) and [Figure 3B](#). The nodal values extracted from this adaptive solution constitute the training dataset for the neural network surrogate, whose loss history is shown in [Figure 3C](#). After 6,000 iterations with Adam, the loss decreases in a fluctuating manner to the order of 10^{-5} and subsequent refinement with L-BFGS further reduces the training error. The trained model is evaluated on a uniform mesh [Figure 3D](#), with the interpolated solution and the corresponding error distribution shown in [Figure 3E](#). While the visual comparison suggests no pronounced deviation, the error plot reveals accuracy limited to the order of 10^{-2} .

Although multilayer perceptrons possess universal approximation capability, the experiments demonstrate that their practical use for mesh-based interpolation faces inherent difficulties. While the networks produce smoother reconstructions, training becomes increasingly demanding with deeper architectures. Furthermore, the non-convexity of the loss landscape often confines optimization to local minima and the error typically stagnates near 10^{-3} , limiting further gains in accuracy. These findings illustrate the challenges of employing fully trainable deep neural networks for functions with pronounced oscillations or sharp gradients. Gradient-based methods entail considerable computational expense and exhibit sensitivity to hyperparameter choices, which complicates their deployment in practice. For interpolation tasks, however, accuracy, efficiency and robustness are all indispensable. This motivates the consideration of alternative strategies, such as extreme learning machines, which provide faster training and more consistent performance.

2.3. Data Transfer via Extreme Learning Machine. As a computationally efficient alternative to fully trainable deep neural networks, the Extreme Learning Machine (ELM) is adopted to construct the surrogate function $\tilde{u}_\theta(\mathbf{x})$. In this framework, the hidden-layer parameters are randomly initialized and kept fixed, whereas the output weights are computed analytically through a closed-form least-squares formulation. Such a design eliminates the need for iterative parameter updates and enables rapid training, making ELM particularly suitable for mesh-based interpolation tasks where efficiency and simplicity are critical.

For a given input $\mathbf{x} \in \mathbb{R}^{d_0}$, the model performs a sequence of nonlinear transformations followed by a linear output mapping:

$$\begin{aligned}\Phi^{(1)}(\mathbf{x}) &= \sigma(\mathbf{W}^{(1)}\mathbf{x} + \mathbf{b}^{(1)}), \\ \Phi^{(2)}(\mathbf{x}) &= \sigma(\mathbf{W}^{(2)}\Phi^{(1)}(\mathbf{x}) + \mathbf{b}^{(2)}), \\ \tilde{u}_\theta(\mathbf{x}) &= \boldsymbol{\beta}^\top \Phi^{(2)}(\mathbf{x}),\end{aligned}$$

where $\mathbf{W}^{(1)} \in \mathbb{R}^{d_1 \times d_0}$ and $\mathbf{W}^{(2)} \in \mathbb{R}^{d_2 \times d_1}$ denote the weight matrices, and $\mathbf{b}^{(1)} \in \mathbb{R}^{d_1}$ and $\mathbf{b}^{(2)} \in \mathbb{R}^{d_2}$ denote the bias vectors. Nonlinearity in the hidden layers is introduced by an element-wise activation function $\sigma(\cdot)$, which can be selected flexibly depending on the application. At the output layer, a parameter vector $\boldsymbol{\beta} \in \mathbb{R}^{d_2}$ serves as the coefficient vector for a linear combination of the hidden features $\Phi^{(2)}(\mathbf{x})$. Aside from $\boldsymbol{\beta}$, the remaining parameters $\{\mathbf{W}^{(1)}, \mathbf{W}^{(2)}, \mathbf{b}^{(1)}, \mathbf{b}^{(2)}\}$ are randomly initialized once and kept fixed during training, so that the optimization reduces to determining $\boldsymbol{\beta}$ via least-squares regression. As shown

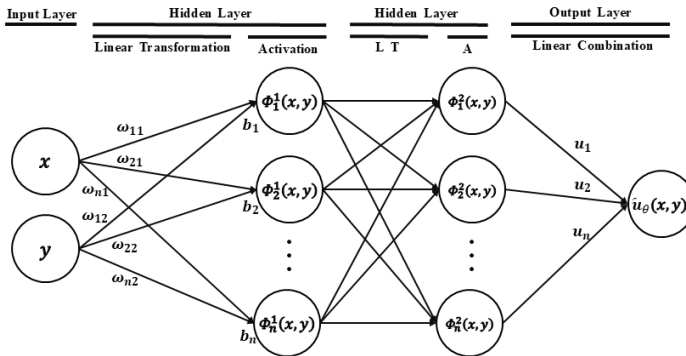


FIGURE 4. Schematic architecture of an extreme learning machine network.

in Figure 4 the architecture follows the neural-network layout introduced previously and differs mainly in its depth. If $\Phi(\mathbf{x}) \in \mathbb{R}^{d_2}$ denotes the composite nonlinear mapping of input \mathbf{x} through the hidden layers, then the ELM prediction takes the simplified form

$$\tilde{u}_\theta(\mathbf{x}) = \boldsymbol{\beta}^\top \Phi(\mathbf{x}).$$

Given a training dataset $\{(\mathbf{x}_i, u_h(\mathbf{x}_i))\}_{i=1}^N$, the nonlinear mapping $\Phi(\mathbf{x}_i)$ of each input is collected into the hidden-layer output matrix $H \in \mathbb{R}^{N \times d_2}$, while the corresponding high-fidelity responses are assembled

into the target vector $U \in \mathbb{R}^N$:

$$H = \begin{bmatrix} \Phi(\mathbf{x}_1)^\top \\ \Phi(\mathbf{x}_2)^\top \\ \vdots \\ \Phi(\mathbf{x}_N)^\top \end{bmatrix}, \quad U = \begin{bmatrix} u_h(\mathbf{x}_1) \\ u_h(\mathbf{x}_2) \\ \vdots \\ u_h(\mathbf{x}_N) \end{bmatrix}.$$

The training of ELM reduces to finding the output weights β that minimize the discrepancy between $H\beta$ and U , namely the standard least-squares problem

$$\beta = \arg \min_{\beta} \|H\beta - U\|_2^2,$$

which admits the closed-form solution

$$\beta = (H^\top H)^{-1} H^\top U. \quad (1)$$

However, the matrix $H^\top H$ may become ill-conditioned or even singular when the number of hidden nodes d_2 is large or when the features in H exhibit strong correlations. This issue can be mitigated by using the Moore–Penrose pseudoinverse or by introducing a regularization term, such as in ridge regression, to ensure numerical stability in the computation of β . The closed-form formulation then enables efficient determination of the output weights without iterative optimization. As a result, both training time and prediction cost are substantially reduced, making ELM a particularly attractive surrogate model when efficiency is critical.

Remark 2.3. *While traditional ELMs typically employ a single hidden layer, the network in this work adopts two hidden layers in order to enhance approximation accuracy while maintaining training stability. This design is motivated by empirical observations rather than theoretical guarantees. In practice, single-layer networks were insufficiently expressive for mesh-based interpolation, whereas additional depth beyond two layers provided no consistent benefit and in some cases introduced instability.*

Example 2.4. *We consider the benchmark functions $u(\mathbf{x})$ introduced in Theorem 2.1, defined on the unit square $[-1, 1]^2$. The experimental setting is given by an ELM architecture $[2, 256, 2500, 1]$ with activation function $\sigma = \sin$, weights $\{W^{(1)}, W^{(2)}, b^{(1)}, b^{(2)}\}$ sampled uniformly from $[-0.4, 0.4]$, and training performed on all source mesh nodes $\{\mathbf{x}_i\}_{i=1}^N$ with responses $\{u(\mathbf{x}_i)\}_{i=1}^N$.*

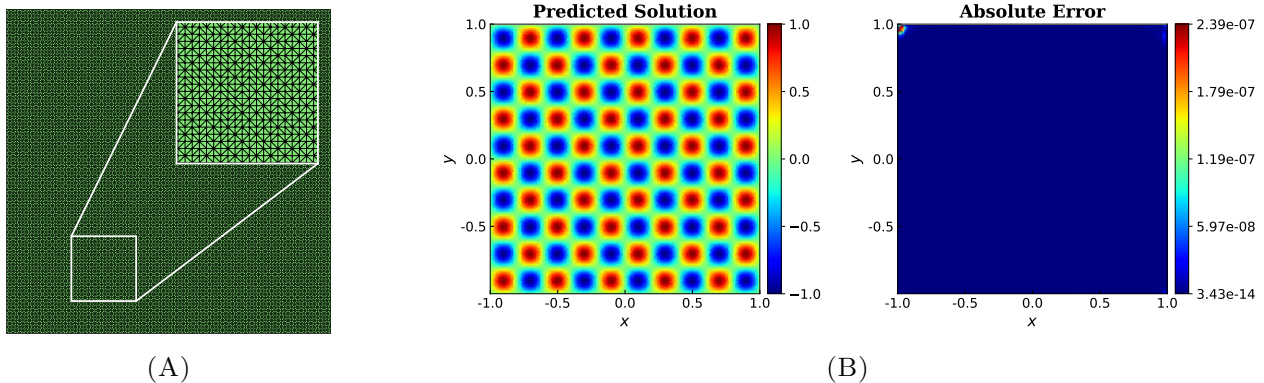


FIGURE 5. Theorem 2.4, ELM interpolation on a quasi-uniform mesh. (A) Test mesh; (B) interpolated solution and error.

Interpolation results on a uniform triangular mesh with 10,000 nodes are displayed in Figure 5. Figure 5A depicts the test mesh, while Figure 5B illustrates the interpolated solution together with the absolute error field. The relative L^2 error is 6.11×10^{-10} and the mean absolute error is 2.14×10^{-11} , representing an improvement of roughly eight orders of magnitude in accuracy compared with the neural network baseline.

It should be emphasized that the reported results are not necessarily optimal, even though the least-squares formulation is convex. The attained accuracy depends on choices such as network architecture, weight initialization¹ and the number of training samples, which are typically determined empirically. These factors may significantly influence performance, and their impact will be further examined in the numerical experiments. Of particular importance is the fact that the initialization distribution exerts no uniform influence while some settings yield stable convergence and others lead to divergence. Even with a fixed network architecture and properly selected initialization, the number of training samples remains a key determinant of accuracy. Accuracy improves as more samples are provided until it saturates or declines beyond the model’s capacity, a behavior that will be shown in the next example.

Example 2.5. *The setup and training data are identical to those of Theorem 2.2.*

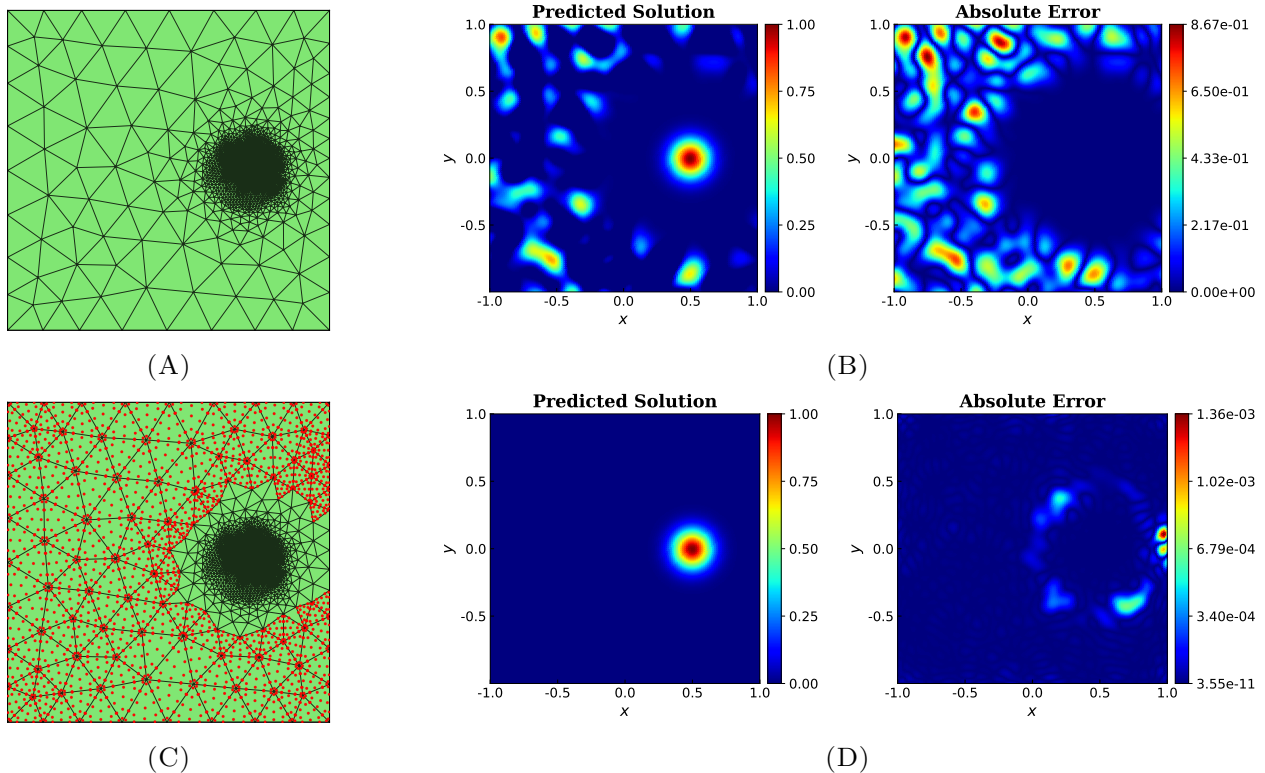


FIGURE 6. Theorem 2.5, ELM interpolation on an adaptive mesh. (A) training mesh; (B) interpolated solution and absolute error on a uniform 100×100 test grid; (C) training mesh with an additional Gaussian point (red); (D) interpolated solution and absolute error.

Adaptive finite element meshes provide an instructive setting to examine how the distribution of training samples influences the performance of ELM-based interpolation. Although adaptive meshes enhance FEM computational efficiency, they pose challenges for ELM-based interpolation. The training samples in Theorem 2.5 are taken from a relatively sparse adaptive mesh characterized by highly nonuniform spatial resolution across the domain (Figure 6A). Despite extensive hyperparameter tuning, the interpolation fails to achieve satisfactory accuracy with an average absolute error of approximately 1.19×10^{-1} . As shown in Figure 6B, the largest errors are concentrated in areas where the mesh nodes are sparsely distributed. This pattern suggests that the limited representation capacity of the model is unevenly distributed throughout the domain, leading to poor generalization in regions with low sampling density. Global approximators, such as ELM, rely on training data that are both informative and sufficiently well-distributed. When nodes are concentrated in finely resolved regions, the model allocates most of its approximation power there, leaving sparsely sampled regions underrepresented. Even though the objective function exhibits smoothness

¹Here “initialization strategy” refers to the probability distribution used to sample the weights, not the random seed.

in those coarse mesh regions, such imbalance still disrupts the restoration of the global structure, thereby giving rise to substantial local errors. These local errors motivated the insertion of extra Gaussian quadrature points within the FEM framework, a natural choice that serves to mitigate bias from nonuniform sampling. Figure 6C displays the adapted training mesh, where red markers denote Gaussian points introduced according to an element-area criterion. These points were allocated to elements with areas above a specified threshold, and their corresponding function values were computed via finite element interpolation. The error distribution in Figure 6D shows that the maximum error has shifted to a region without Gaussian points refinement, and the overall accuracy has improved by approximately four orders of magnitude, with an average absolute error of 2.52×10^{-5} . Unfortunately, this remedy is ultimately impractical. The reported result, achieved after extensive manual parameter tuning, depends critically on a well-chosen network architecture and proper parameter initialization for the additional sampling to be effective. The error distribution in Figure 6D shows that the maximum error has shifted to a region without Gaussian refinement, and the overall accuracy has improved by approximately four orders of magnitude, with an average absolute error of 2.52×10^{-5} . Unfortunately, this remedy is ultimately impractical. The reported result was obtained with a network configuration of [2, 128, 1024, 1], uniformly initialized weights in $[-0.7, 0.7]$, and sixteen Gaussian points added to each element whose area exceeded 0.007. It depends critically on a well-chosen network architecture and proper parameter initialization for the additional sampling to be effective. Our attempts to extend this manual procedure into a fully adaptive sample enrichment strategy proved extremely difficult. There is no reliable mechanism to control element selection or the growth of training points, nor a clear criterion for determining when the process should terminate. Moreover, adaptive point enrichment in fact does not truly enhance the network’s expressive capacity. Perhaps, it is the adaptivity of the network architecture itself that ultimately holds the key to genuine adaptivity.

2.4. Data Transfer via Radial Basis Function-ELM. The ELM framework can be extended naturally to the radial basis function (RBF) network case yielding a simplified variant named the RBF-ELM. The model combines a radial-basis feature map with a least-squares output layer, where each input activates only a few localized units leading to reduced sensitivity to training-point distribution and a simpler network structure. This formulation was first formalized by Broomhead and Lowe [5] for multivariate functional interpolation and later reinterpreted by Moody and Darken [20] within the neural-network framework where it gained broad recognition. The theoretical analysis by Poggio and Girosi [12] further established that RBF networks possess strong approximation capabilities for continuous functions. Concretely, the functional form of the RBF mapping can be written as follows. Given an input point $\mathbf{x} \in \mathbb{R}^{d_0}$, its mapping is defined by d_1 Gaussian kernels whose centers $\{\mathbf{c}_j\}_{j=1}^{d_1} \subset \mathbb{R}^{d_0}$ may be determined by uniform placement, random sampling, or clustering (e.g., k -means). The j -th feature then takes the form

$$\phi_j(\mathbf{x}) = \exp\left(-\frac{\|\mathbf{x} - \mathbf{c}_j\|^2}{\varepsilon^2}\right), \quad j = 1, \dots, d_1,$$

where the shape parameter $\varepsilon > 0$ specifies the width of each basis function. Each Gaussian kernel acts as a localized basis that is analogous to finite element basis functions. This locality allows the model to adapt to variations in node distribution and remain effective even when samples are not uniformly placed. Collecting these features gives $\Phi(\mathbf{x}) \in \mathbb{R}^{d_1}$ which provides the input representation for the output layer:

$$\tilde{u}_\theta(\mathbf{x}) = \beta^\top \Phi(\mathbf{x}),$$

with coefficients $\beta \in \mathbb{R}^{d_1}$ obtained via the regularized least-squares formulation introduced in Equation (1). The overall architecture is illustrated in Figure 7, where *measure offset* denotes the distance to the kernel centers and *activation* refers to the application of the exponential function.

Example 2.6. We now revisit the singular function test case introduced earlier where the standard ELM model failed to provide satisfactory interpolation due to non-uniform sampling.

As shown in Figure 8, the RBF model significantly improves upon the basic ELM architecture, particularly in regions with sparse training data. The model used here adopts the structure [2, 300, 1] and shape parameter $\varepsilon = 60$, where 300 RBF centers are randomly sampled over the domain. The absolute error is greatly reduced across the domain, including in sparsely sampled regions.

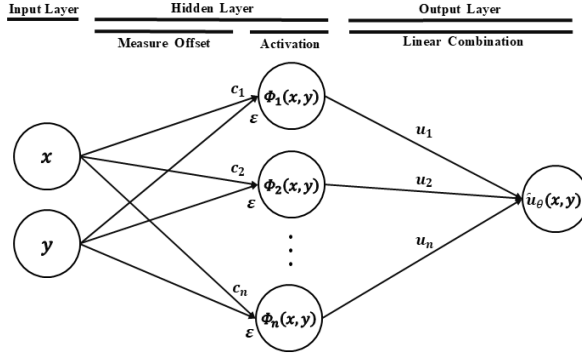


FIGURE 7. Schematic architecture of a RBF-ELM network.

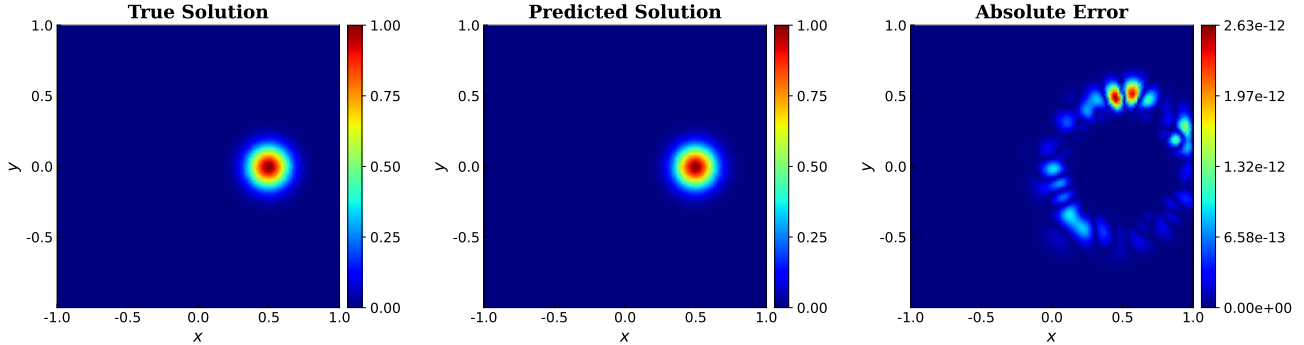


FIGURE 8. Interpolated solution and corresponding absolute error distribution for the singular function test case.

Table 1 illustrates the contrasting characteristics of FNN, ELM, and RBF-ELM when applied to mesh-based data transfer. FNN models can handle arbitrary meshes and deliver stable interpolation, yet their training remains iterative and costly, and accuracy typically plateaus at a relative error of about 10^{-3} . ELM achieves near machine precision with minimal training cost, but this advantage holds only under uniform sampling, as its performance deteriorates sharply with irregular data distributions. RBF-ELM strikes a balance between these two extremes: it maintains competitive accuracy at negligible training cost and shows reduced sensitivity to initialization and mesh irregularities, making it a practical compromise for inter-grid prediction tasks.

TABLE 1. Performance trade-offs among surrogate models for mesh-based data transfer.

Model	Mesh Compatibility	Computational Cost	Precision	Robustness
FNN	Arbitrary	High	Low (10^{-3} – 10^{-4})	Moderate
ELM	Uniform	Low	Moderate (10^{-6} – 10^{-9})	Low
RBF-ELM	Arbitrary	Low	High (10^{-10} – 10^{-14})	High

3. APPLICATION

Data interpolation among multiple meshes with varying topology or resolution is a fundamental operation in many multi-physics and adaptive simulation workflows. Maintaining field continuity and ensuring smooth transitions across successive mappings is particularly challenging, especially when dealing with

unstructured meshes. The results in this section show that the model effectively maintains field continuity and accuracy even after multiple iterations, making it a reliable tool for simulations requiring frequent mesh updates. Without loss of generality, we illustrate this process by iterative interpolation between two non-matching meshes as a representative case, demonstrating the model’s ability to preserve accuracy and produce smooth reconstructions across repeated transfers.

The iterative procedure is initialized with two training sets derived from a reference solution u :

$$\mathcal{D}_A^{(0)} = \{(\mathbf{x}, u(\mathbf{x})) : \mathbf{x} \in \mathcal{N}_A\}, \quad \mathcal{D}_B^{(0)} = \{(\mathbf{x}, u(\mathbf{x})) : \mathbf{x} \in \mathcal{N}_B\}.$$

For $k = 0, 1, 2, \dots$, the cycle is defined as follows:

- (i) $\mathcal{T}_A \rightarrow \mathcal{T}_B$. Train $\tilde{u}_{\theta_A^{(k)}}$ on $\mathcal{D}_A^{(k)}$, then evaluate at the node set \mathcal{N}_B to obtain

$$\mathcal{D}_B^{(k+1)} = \{(\mathbf{x}, \tilde{u}_{\theta_A^{(k)}}(\mathbf{x})) : \mathbf{x} \in \mathcal{N}_B\},$$

where $\tilde{u}_{\theta_A^{(k)}}$ denotes the RBF-ELM surrogate model for \mathcal{T}_A at iteration k parameterized by θ .

- (ii) $\mathcal{T}_B \rightarrow \mathcal{T}_A$. Train $\tilde{u}_{\theta_B^{(k+1)}}$ on $\mathcal{D}_B^{(k+1)}$, then evaluate at \mathcal{N}_A to obtain

$$\mathcal{D}_A^{(k+1)} = \{(\mathbf{x}, \tilde{u}_{\theta_B^{(k+1)}}(\mathbf{x})) : \mathbf{x} \in \mathcal{N}_A\}.$$

Repeating (i)–(ii) generates the alternating sequence

$$\mathcal{D}_A^{(0)} \rightarrow \mathcal{D}_B^{(1)} \rightarrow \mathcal{D}_A^{(1)} \rightarrow \dots \rightarrow \mathcal{D}_B^{(k)} \rightarrow \mathcal{D}_A^{(k)}.$$

Example 3.1. As mentioned in [Theorem 2.1](#), the piecewise-linear interpolation method is limited in its ability to preserve high-frequency components and curvature under repeated transfers between non-matching meshes.

After numerous alternating transfers between \mathcal{T}_A and \mathcal{T}_B , the solution in 1D gradually approaches a straight line, while in 2D it becomes locally flat. The impact of this progressive smoothing on solution accuracy is demonstrated in [Figure 9](#) using the 1D reference function $u(x) = \sin(\pi x)$. In this test, RBF-ELM interpolation uses $N_c = 100$ centers randomly drawn from the training data under a shape parameter $\varepsilon = 100$. The blue line in the figure shows the pointwise absolute error for data transferred from \mathcal{T}_A to \mathcal{T}_B , while the orange line corresponds to the reverse transfer. Here, \mathcal{T}_A is uniformly discretized over $[0, 1]$ with 100 points, and \mathcal{T}_B is generated by combining the midpoints of all elements in \mathcal{T}_A with the boundary nodes at $x = 0$ and $x = 1$. After 100 iterations of back-and-forth interpolation, the RBF-ELM method achieves 10^{-8} precision, surpassing the standard method’s 10^{-2} accuracy by a significant margin. [Figure 9C](#) shows the evolution of the error with respect to the number of iterations. Although the error increases for both methods, the rate of increase for the standard interpolation method is notably faster.

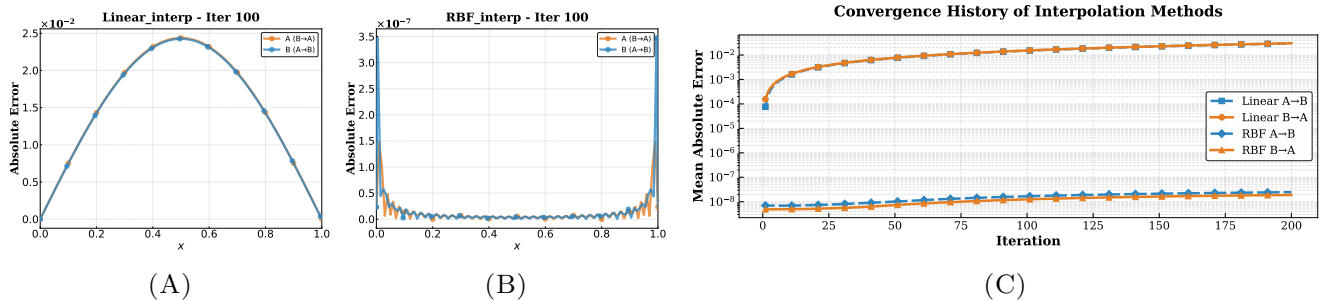


FIGURE 9. Comparison of piecewise linear interpolation and the RBF-ELM interpolation model for a smooth 1D function. (A) Error of piecewise linear interpolation after 100 iterations; (B) Error of RBF-ELM interpolation after 100 iterations; (C) Error evolution history over transfer iterations.

Example 3.2. The behavior described above becomes even more pronounced when the reference solution is a multi-peak function. Consider the following mixture of two Gaussian functions:

$$u(x) = \exp(-400(x - 0.35)^2) - \exp(-200(x - 0.75)^2) / 2.$$

The detailed evolution of the interpolation process for this multi-peak function is illustrated in Figure 10. In this figure, the black curve represents the reference solution, while the orange and blue markers correspond to the nodal points of the meshes \mathcal{T}_A and \mathcal{T}_B , respectively. Thick and thin lines differentiate between the two interpolation directions, where thin lines indicate solutions obtained from thick lines. Starting from a smoothly varying initial field (Figure 10A), each alternating transfer between \mathcal{T}_A and \mathcal{T}_B slightly distorts the profile and reduces curvature. After five cycles (Figure 10B), the field becomes visibly flatter, reflecting the cumulative smoothing effect of repeated linear interpolation across non-matching meshes. As the process continues to 25 and 100 iterations (Figure 10C–Figure 10D), the oscillatory features are almost completely lost, and the solution gradually converges toward a straight line. However, in the case of RBF-ELM interpolation, even after 200 iterations, the error remains imperceptible to the naked eye, as shown in Figure 11A. A comparative assessment of the error convergence behavior for both interpolation approaches is provided in Figure 11B.

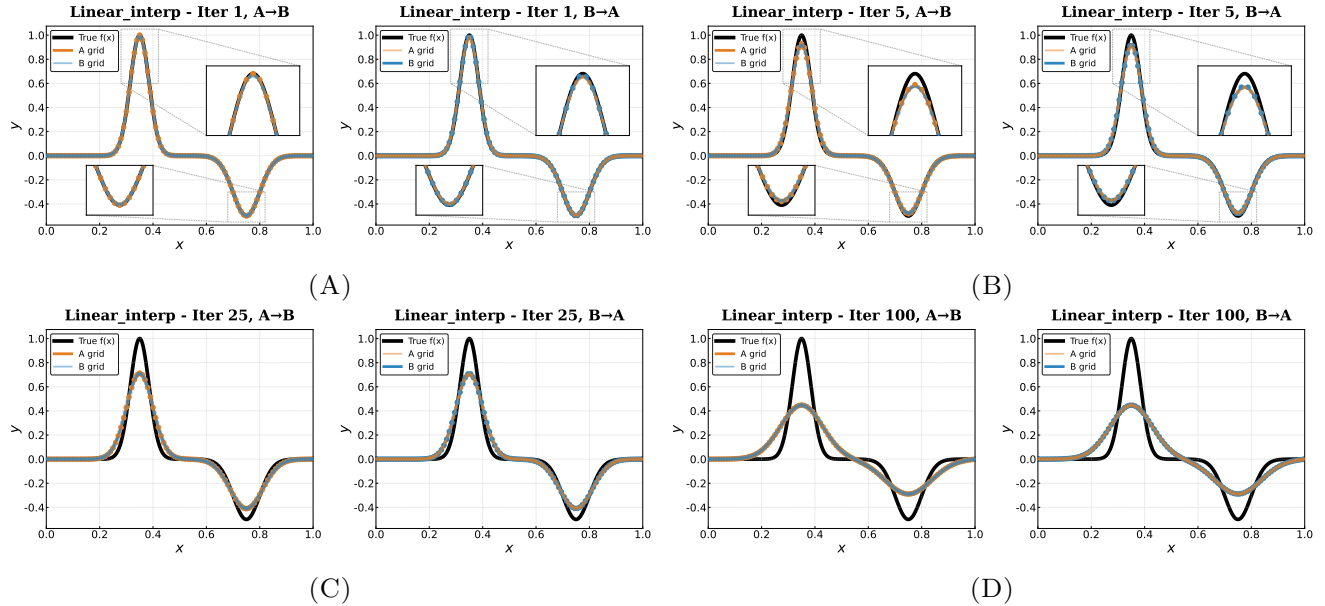


FIGURE 10. Piecewise linear interpolation results for a 1D multi-peak problem. (A)–(D) Interpolated solutions after 1, 5, 25, and 100 transfer iterations.

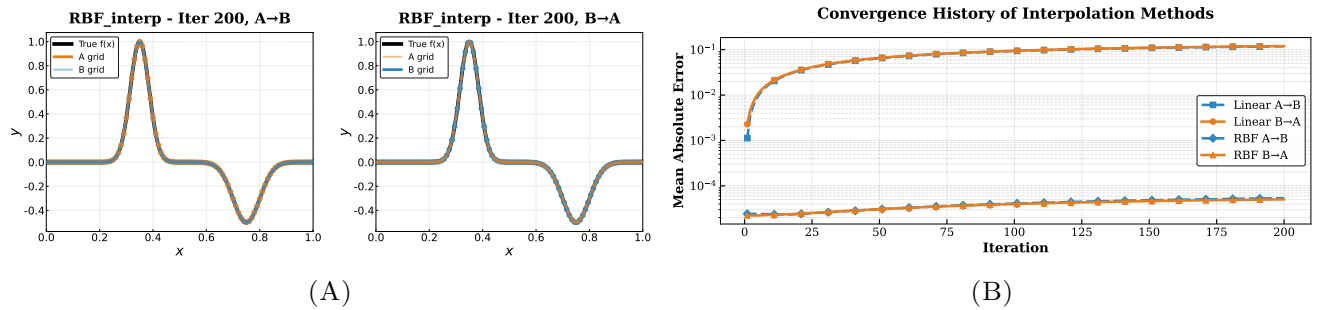


FIGURE 11. RBF-ELM interpolation performance and iterative error on multi-peak function. (A) Interpolated solution after 200 iterations; (B) Error evolution history over transfer iterations.

Example 3.3. *Extend the same iterative transfer procedure to the two-dimensional case for further assessment. What we used in the interpolation procedure is a uniform triangular mesh \mathcal{T}_A with 10,000 nodes and a Delaunay triangular mesh \mathcal{T}_B , as shown in Figure 12A and Figure 12B. The latter is constructed from the midpoints of \mathcal{T}_A elements and boundary nodes, thus typically having about twice as many nodes as \mathcal{T}_A .*

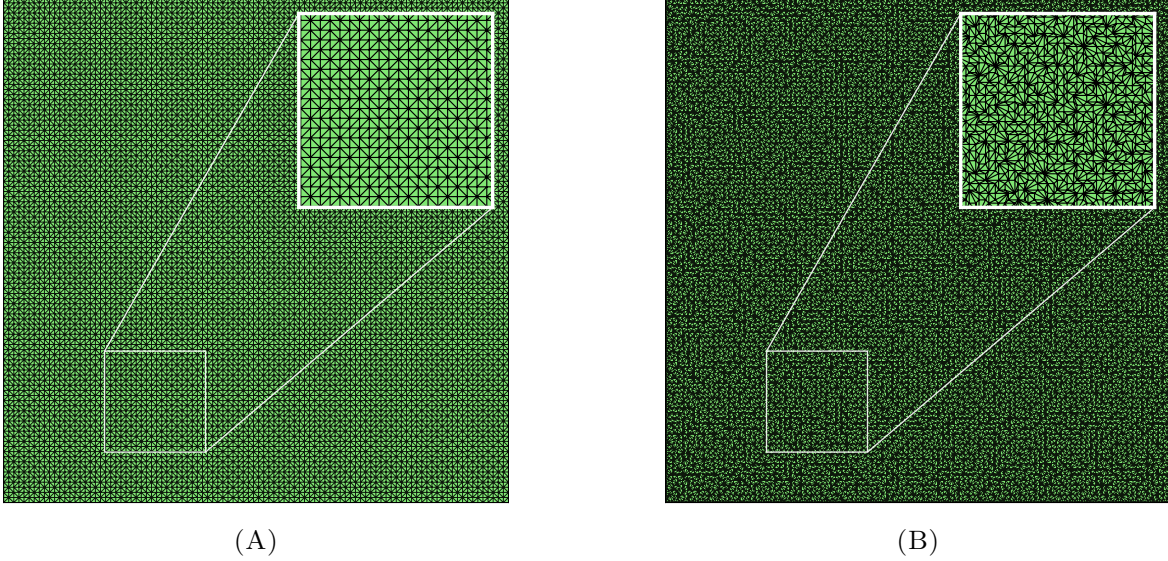


FIGURE 12. Mesh configuration for 2D interpolation. (A) Uniform triangular mesh \mathcal{T}_A ; (B) Delaunay triangular mesh \mathcal{T}_B .

Benchmarking starts with the smooth reference solution $u(x, y) = -x^2 - y^2$ on $[-1, 1]^2$, illustrated in Figure 13A. In what follows, we employ an RBF-ELM configuration with $N_c = 1000$ centers randomly drawn from the training samples and a shape parameter $\varepsilon = 10$. The error maps after 100 transfer iterations for the piecewise linear interpolation and the RBF-ELM method are presented in Figure 13C and Figure 13D, respectively. In which the piecewise linear interpolation yields lower errors on the boundaries while substantial interior errors, yielding a global mean absolute error on the order of 10^{-2} . In contrast, the RBF-ELM model confines errors to the domain corners and achieves a global accuracy on the order of 10^{-7} even with arbitrarily chosen centers and shape parameter, indicating substantial potential for further improvement. This performance gap remains consistent over successive iterations, as evidenced by the error evolution shown in Figure 13.

Example 3.4. *Increased frequency content in the reference function further amplifies the advantage of RBF-ELM in delivering high accuracy and numerical stability in interpolation. Consider the reference function*

$$u(x, y) = \sin(\pi x) \sin(\pi y) \left[\sin(6\pi x) \cos(4\pi y) + 0.6 \sin(8\pi(x-0.3)) \cos(6\pi(y+0.2)) - 0.4 \cos(10\pi x) \sin(8\pi y) \right],$$

where the outer term $\sin(\pi x) \sin(\pi y)$ ensures that the function vanishes on the domain boundary and forms a smooth multi-peak profile inside the domain, as illustrated in Figure 14A. All settings were identical to the previous example, except for a change in the RBF-ELM shape parameter to $\varepsilon = 50$.

Figure 15A shows the result obtained by piecewise linear interpolation after 25 iterations that exhibits clear degradation of structural detail. It almost collapses into a flat surface after 100 iterations, as shown in Figure 15B. In contrast, the RBF-ELM model exhibits a markedly different behavior: even after 25 (Figure 15C) and 100 (Figure 15D) iterations, it retains the overall shape and fine variations of the original field with little degradation. The interpolation errors of the two methods in successive transfer iterations are compared in Figure 14B. Overall, although the errors of both methods increase with repeated transfers, the growth rate of the piecewise linear interpolation is markedly higher than that of the RBF-ELM model.

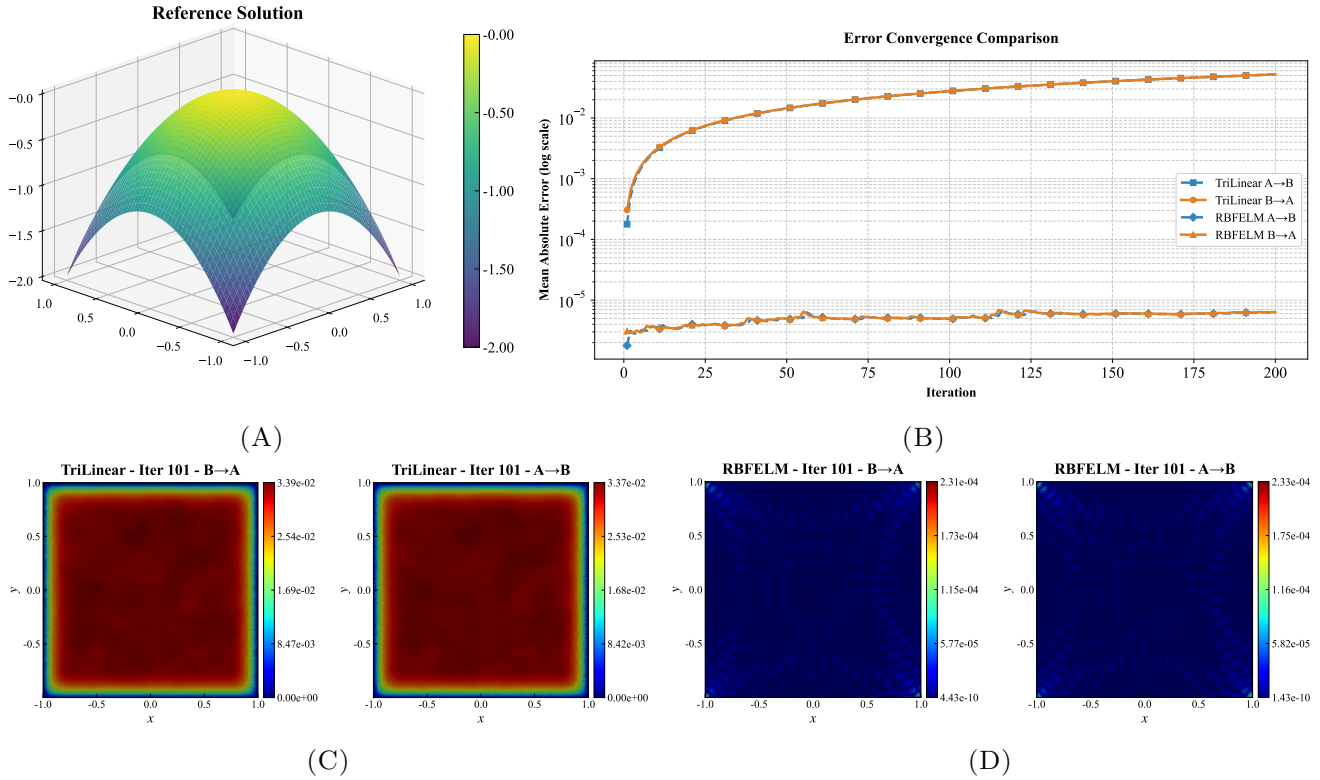


FIGURE 13. Evolution and spatial distributions of interpolation errors for a smooth 2D problem. (A) Reference solution; (B) Error evolution history over transfer iterations; (C) Piecewise linear interpolated error after 100 iterations; (D) RBF-ELM interpolated error after 100 iterations.

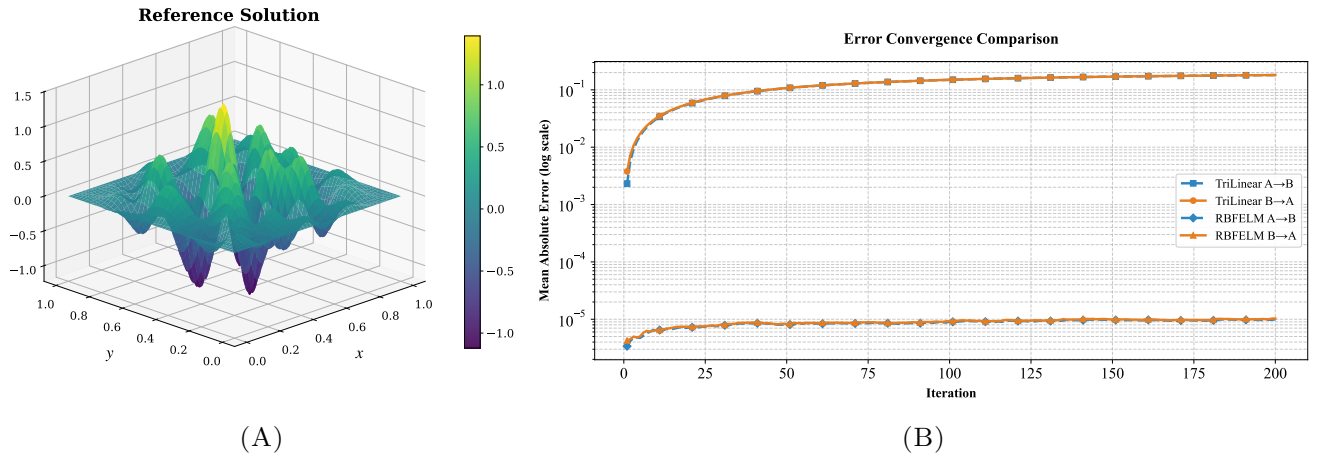


FIGURE 14. Convergence behavior of interpolation errors for a 2D multi-peak problem. (A) Reference solution; (B) Error evolution history over transfer iterations.

4. CONCLUSIONS

This work presents an examination of three interpolation strategies for transferring function data across unstructured meshes and an analysis of their respective trade-offs. The FNN data transform method provides stable interpolation and moderate generalization across test cases, though its performance is limited to an accuracy around 10^{-3} alongside high computational cost from iterative training. Addressing these

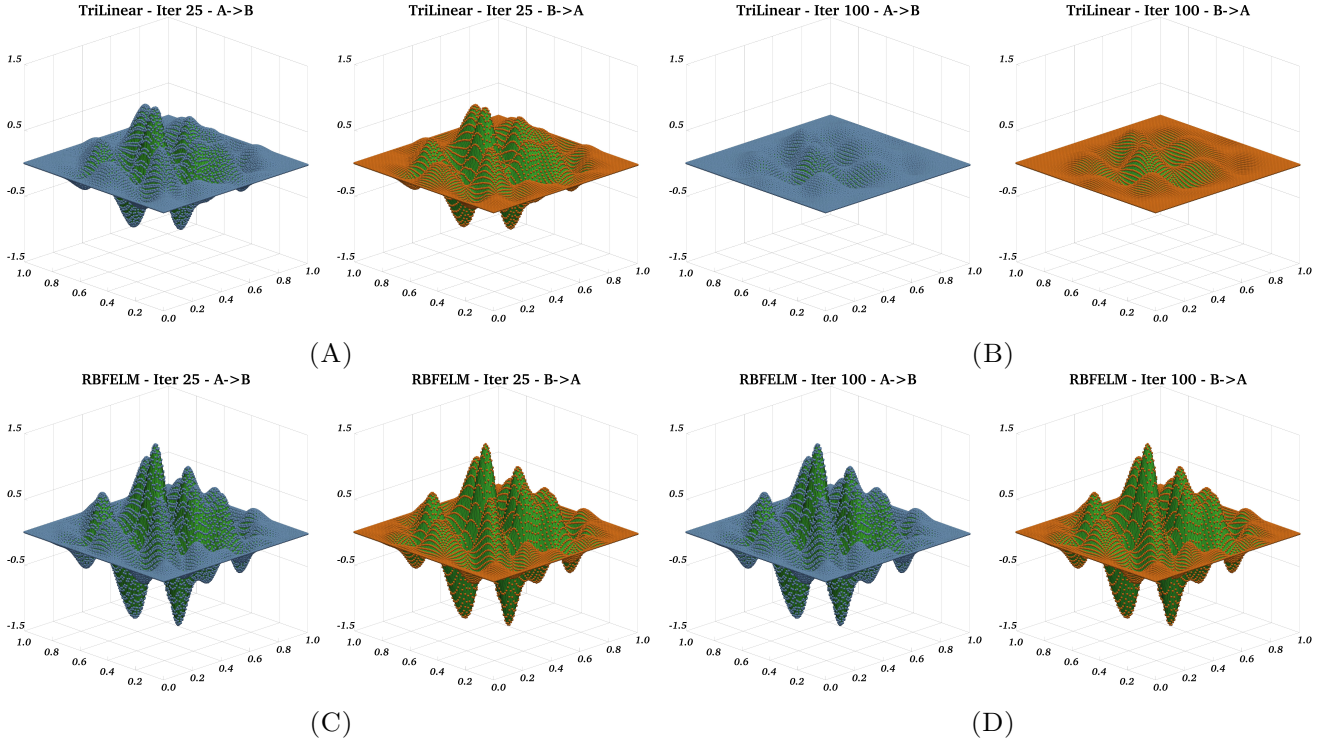


FIGURE 15. Comparison of piecewise linear and RBF-ELM interpolation results. (A)-(B) piecewise linear interpolation results after 25 and 100 iterations; left/right subplots correspond to transfers $\mathcal{T}_A \rightarrow \mathcal{T}_B$ and $\mathcal{T}_B \rightarrow \mathcal{T}_A$, respectively; (C)-(D) RBF-ELM results after 25 and 100 iterations.

limitations, the ELM approach achieves substantially higher accuracy with minimal training cost. However, this advantage is accompanied by a marked sensitivity to the network architecture, initialization, and sample distribution. While augmenting the training set with Gaussian points in sparse regions can alleviate sample sensitivity, it introduces new approximation errors and lacks a systematic stopping criterion. The RBF-ELM data transfer approach strikes an effective balance between accuracy, computational efficiency, and ease of implementation. It exhibits reduced sensitivity to hyperparameter selection and improved robustness under irregular sampling, making it a practical choice for mesh-based interpolation tasks. By directly computing a global approximation mapping coordinates to solution values, the model avoids expensive training and bypasses the need for explicit mesh connectivity, allowing fast and flexible evaluations at arbitrarily distributed points. Even on adaptive meshes, it maintains a distinct accuracy advantage over the previous two approaches. These features make the RBF-ELM approach particularly suitable for dynamic or adaptive simulations that require frequent mesh updates and data transfer. Finally, we applied the method to multiple data transfers and achieved significant results in preserving long-term accuracy and robustness, a capability beyond the reach of conventional interpolation schemes. We also observed that randomly selecting center locations has a negligible impact when the number of centers and the shape parameter are held fixed. However, the hyperparameters used in the previous section were not rigorously tuned, which is one of the limitations of this study. A systematic analysis of the effects of the number of RBF centers and shape parameters is essential for further improving transfer accuracy. Additionally, the RBF-ELM model shows potential as an effective tool for future multiphysics applications, particularly in maintaining long-term fidelity through the preservation of integral quantities such as mass, momentum, and energy across mesh transfers. These aspects will be explored in future research to further enhance the performance of the method and broaden its applicability.

ACKNOWLEDGMENTS

This research was supported by the National Key R&D Program of China (2024YFA1012600) and NSFC Project (12431014).

REFERENCES

- [1] Oleg Antonić, Josip Krizan, Antun Marki, and Dragan Bukovec. Spatio-temporal interpolation of climatic variables over large region of complex terrain using neural networks. *Ecological Modelling*, 138(1–3):255–263, March 2001.
- [2] Ferdinando Auricchio, Maria Roberta Belardo, Francesco Calabrò, Gianluca Fabiani, and Ariel F. Pascaner. On the accuracy of interpolation based on single-layer artificial neural networks with a focus on defeating the runge phenomenon. *Soft Computing*, 28(20):11767–11785, July 2024.
- [3] Ivo Babuška and Theofanis Strouboulis. *The Finite Element Method and its Reliability*. Oxford University Press Oxford, August 2001.
- [4] Wolfgang Bangerth and Rolf Rannacher. *Adaptive Finite Element Methods for Differential Equations*. Birkhäuser Basel, 2003.
- [5] David S. Broomhead and David Lowe. Multivariable functional interpolation and adaptive networks. *Complex Syst.*, 2:321–355, 1988.
- [6] Michele Bucelli, Francesco Regazzoni, Luca Dede’, and Alfio Quarteroni. Robust radial basis function interpolation based on geodesic distance for the numerical coupling of multiphysics problems. *SIAM Journal on Scientific Computing*, 46(6):B981–B1002, December 2024.
- [7] Xinhai Chen, Rongliang Chen, Qian Wan, Rui Xu, and Jie Liu. An improved data-free surrogate model for solving partial differential equations using deep neural networks. *Scientific Reports*, 11(1), September 2021.
- [8] Zhixiang Chen and Feilong Cao. Scattered data approximation by neural networks operators. *Neurocomputing*, 190:237–242, May 2016.
- [9] G. Cybenko. Approximation by superpositions of a sigmoidal function. *Mathematics of Control, Signals, and Systems*, 2(4):303–314, December 1989.
- [10] Victorita Dolean, Pierre Jolivet, and Frédéric Nataf. *An Introduction to Domain Decomposition Methods: Algorithms, Theory, and Parallel Implementation*. Society for Industrial and Applied Mathematics, November 2015.
- [11] C. Farhat, M. Lesoinne, and P. Le Tallec. Load and motion transfer algorithms for fluid/structure interaction problems with non-matching discrete interfaces: Momentum and energy conservation, optimal discretization and application to aeroelasticity. *Computer Methods in Applied Mechanics and Engineering*, 157(1–2):95–114, April 1998.
- [12] F. Girosi and T. Poggio. Networks and the best approximation property. *Biological Cybernetics*, 63(3):169–176, July 1990.
- [13] Jiexiong Hao, Yunqing Huang, Nianyu Yi, and Peimeng Yin. Neural network-enhanced hr -adaptive finite element algorithm for parabolic equations, 2025.
- [14] Helmut Harbecht, Michael Multerer, and Jacopo Quizi. The dimension weighted fast multipole method for scattered data approximation. *Journal of Computational Physics*, 532:113956, July 2025.
- [15] Guang-Bin Huang, Qin-Yu Zhu, and Chee-Kheong Siew. Extreme learning machine: Theory and applications. *Neurocomputing*, 70(1–3):489–501, December 2006.
- [16] P. Lancaster and K. Salkauskas. Surfaces generated by moving least squares methods. *Mathematics of Computation*, 37(155):141–158, 1981.
- [17] Jichun Li and C.S. Chen. A simple efficient algorithm for interpolation between different grids in both 2d and 3d. *Mathematics and Computers in Simulation*, 58(2):125–132, January 2002.
- [18] B. Llanas and F.J. Sainz. Constructive approximate interpolation by neural networks. *Journal of Computational and Applied Mathematics*, 188(2):283–308, April 2006.
- [19] J. R. Maddison and H. R. Hiester. Optimal constrained interpolation in mesh-adaptive finite element modeling. *SIAM Journal on Scientific Computing*, 39(5):A2257–A2286, January 2017.
- [20] John Moody and Christian J. Darken. Fast learning in networks of locally-tuned processing units. *Neural Computation*, 1(2):281–294, June 1989.
- [21] Ricardo H. Nochetto, Kunibert G. Siebert, and Andreas Veiser. *Theory of adaptive finite element methods: An introduction*, page 409–542. Springer Berlin Heidelberg, 2009.
- [22] N. Plaziac. Image interpolation using neural networks. *IEEE Transactions on Image Processing*, 8(11):1647–1651, 1999.
- [23] Zhongang Qi, Tianchun Wang, Guojie Song, Weisong Hu, Xi Li, and Zhongfei Zhang. Deep air learning: Interpolation, prediction, and feature analysis of fine-grained air quality. *IEEE Transactions on Knowledge and Data Engineering*, 30(12):2285–2297, December 2018.
- [24] Juan P. Rigol, Claire H. Jarvis, and Neil Stuart. Artificial neural networks as a tool for spatial interpolation. *International Journal of Geographical Information Science*, 15(4):323–343, June 2001.
- [25] Holger Wendland. *Scattered Data Approximation*. Cambridge University Press, December 2004.
- [26] Zhou Yang, Yuwang Xu, Jionglin Jing, Xuepeng Fu, Bofu Wang, Haojie Ren, Mengmeng Zhang, and Tongxiao Sun. Investigation of physics-informed neural networks to reconstruct a flow field with high resolution. *Journal of Marine Science and Engineering*, 11(11):2045, October 2023.

- [27] Guangcai Yin, Xingling Chen, Hanghai Zhu, Zhiliang Chen, Chuanghong Su, Zechen He, Jinrong Qiu, and Tieyu Wang. A novel interpolation method to predict soil heavy metals based on a genetic algorithm and neural network model. *Science of The Total Environment*, 825:153948, June 2022.
- [28] Mo Zhang, Wenjiao Shi, and Ziwei Xu. Systematic comparison of five machine-learning models in classification and interpolation of soil particle size fractions using different transformed data. *Hydrology and Earth System Sciences*, 24(5):2505–2526, May 2020.

† HUNAN KEY LABORATORY FOR COMPUTATION AND SIMULATION IN SCIENCE AND ENGINEERING, SCHOOL OF MATHEMATICS AND COMPUTATIONAL SCIENCE, XIANGTAN UNIVERSITY, XIANGTAN 411105, HUNAN, P.R.CHINA
Email address: moodbear@qq.com (J. Hao); yiniany@xtu.edu.cn (N. Yi)

§ NATIONAL CENTER FOR APPLIED MATHEMATICS IN HUNAN, KEY LABORATORY OF INTELLIGENT COMPUTING & INFORMATION PROCESSING OF MINISTRY OF EDUCATION, XIANGTAN UNIVERSITY, XIANGTAN 411105, HUNAN, P.R.CHINA
Email address: huangyq@xtu.edu.cn